

Defects Classification via Hierarchical Graph Convolutional Network in L-PBF Additive Manufacturing

Anyi Li*, Jia Liu*‡, Shuai Shao†‡, Nima Shamsaei†‡

*Department of Industrials and Systems Engineering, Auburn University, Auburn, AL 36849

†Department of Mechanical Engineering, Auburn University, Auburn, AL 36849

‡National Center of Additive Manufacturing Excellence (NCAME), Auburn University, Auburn, AL 36849

Abstract

Three typical types of defects, i.e., keyholes, lack of fusion (LoF), and gas-entrapped pores (GEP), characterized by various features (e.g., volume, surface area, etc.), are generated under different process parameters of laser beam powder bed fusion (L-PBF) processes in additive manufacturing (AM). The different types of defects deteriorate the mechanical performance of L-PBF components, such as fatigue life, to a different extent. However, there is a lack of recognized approaches to classify the defects automatically and accurately in L-PBF components. This work presents a novel hierarchical graph convolutional network (H-GCN) to classify different types of defects by a cascading GCN structure with a low-level feature (e.g., defect features) layer and a high-level feature (e.g., process parameters) layer. Such an H-GCN not only leverages the multi-level information from process parameters and defect features to classify the defects but also explores the impact of process parameters on defect types and features. The H-GCN is evaluated through a case study with X-ray computed tomography (CT) L-PBF defect datasets and compared with several machine learning methods. H-GCN exhibits an outstanding classification performance with an F1-score of 1.000 and reveals the potential effect of process parameters on three types of defects.

Keywords: Laser beam powder bed fusion, X-ray CT, Hierarchical graph convolutional network, Defects classification.

Introduction

As a promising disruptive technology, additive manufacturing (AM), which creates lightweight 3D components with intricate geometries using layer-wise strategy directly from solid digital models, is evolving from rapid prototyping to revolutionary digital manufacturing technology [1-3]. Laser beam powder bed fusion (L-PBF) is one of the metal AM processes that has enormous potential to fabricate parts with complex geometry for functional and structural applications in different industries, such as aerospace and automotive [4, 5]. However, the complex dynamics such as high dynamic molten pool, ultra-high solidification/cooling rate, or large thermal gradient caused by the variability of process parameters like laser power, scanning speed, hatch spacing, and layer thickness [6] will inevitably generate defects in the inner structure of L-PBF components. These different types of defects, such as keyhole porosity, lack of fusion (LoF) pores, and gas entrapped pores (GEP), can serve as crack initiation sites under cyclic loading [7-9] of fatigue life, which can lead to failure of L-PBF components [10-12]. Therefore, it is important to identify such critical defects and prevent crack initiation to reduce the chance of fracture in L-PBF components.

Moreover, research on defect classification of L-PBF components with new defect characterization has gained tremendous traction. Defect features, such as volume, surface area, aspect ratio, and sphericity, extracted from X-ray computed tomography (CT) 3D data are of great help to understand different types of defects in L-PBF components. A novel classification method is urgently needed to automatically classify defects of L-PBF components for high accuracy and efficiency with a massive amount of data available [13]. In summary, there are three critical issues to be resolved in this paper: (1) How to utilize multi-level information to explore process parameters' impact on different types of defects in the L-PBF components? (2) How to characterize the property or features of different types of defects in the L-PBF components? (3) How to automatically classify defects of L-PBF components to avoid a complicated manual classification process? The rest of this paper is organized as follows: the proposed H-GCN for defect classification is detailed in Section methodology; further experiment of H-GCN with a real case study on the defect classification of L-PBF components in Section case study; finally, conclusions and future research topics are summarized in the final Section.

Methodology

This work aims to develop a novel hierarchical graph convolutional network (H-GCN) for automatic defects classification in L-PBF components and quantify the impact of process parameters on the generation of different types of defects in L-PBF components. This model incorporates process parameters into a GCN unit on its high level and then combines the defect features extracted by content-based image retrieval (CBIR) technique from 3D X-ray CT data and output of the high-level GCN unit into a low-level GCN to classify three types of defects, i.e., keyhole porosity, LoF pores, and GEP of L-PBF components. Meanwhile, the hierarchical structure can also shed some light on the impact of process parameters on the generation of different defect types. The framework of the overall research methodology is summarized in Figure 1.

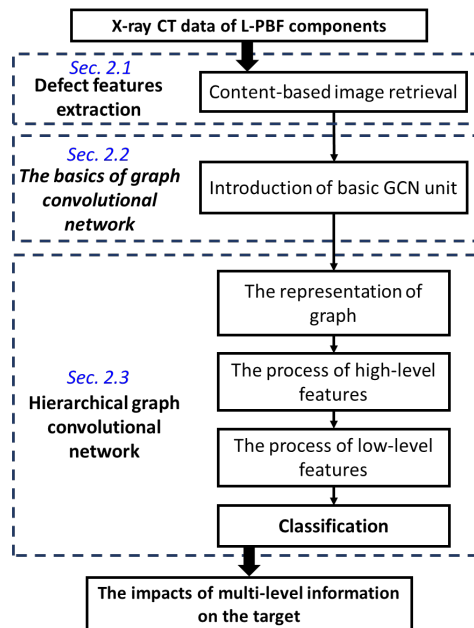


Figure 1. Overall method of H-GCN for defect classification of L-PBF components.

Defect features extraction

Content-based image retrieval (CBIR) is one of the computer vision techniques which can characterize defects on 2D fractography images [14, 15] and 3D X-ray CT scans. All the extracted defect features are summarized in Table 1 with their corresponding descriptions. Apart from traditional features such as volume, surface area, and major axis length, other "untraditional" features can also reveal defect characteristics. For example, solidity can be used to measure whether the shape of a defect is convex and compact with an irregular shape; sphericity is the ratio of the surface area of a sphere to the surface area of the particle [16]; sparseness is the ratio between the volume of ellipsoid and volume of the object. The illustration of defect features for keyhole, LoF, and GEP can be seen in Figure 2. These defect features can be used as one of the input components of the proposed H-GCN in this study.

Table 1. Defect features from X-ray CT data of L-PBF components.

	Representations	Definition
Basics for defect features	Minor axis length	a
	Major axis length	b
	Length along z-axis	c
	Convex area	S_c
	Volume	V_e
	Surface area	S_a
	Max axis length	L
	Aspect ratio	$\frac{b}{a}$
	Sphericity	$\frac{\text{The surface area of a sphere}}{S}$
	Solidity	$\frac{S_a}{S_c}$
Descriptors (Features)	Equivalent diameter	$d = 2\sqrt[3]{\frac{3V_e}{4\pi}}$ [17]
	Roundness	$R = \frac{4S_a}{\pi b^2}$
	Extent	D_f^{Min}
	Sparseness	$\frac{\text{The surface area of a sphere}}{S_a}$
	Elongation	$\frac{a}{b}$
	Flatness	$\frac{b}{c}$

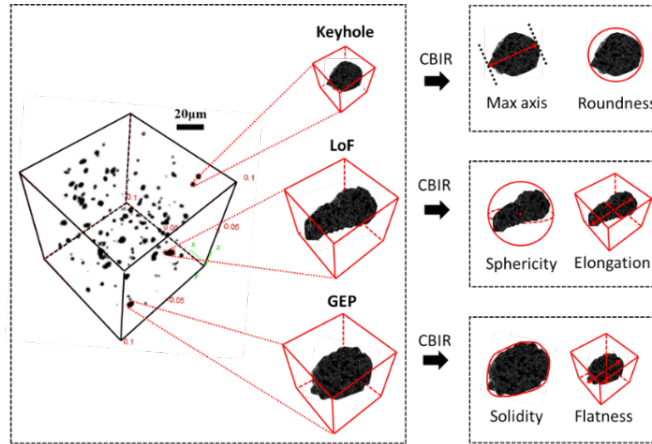


Figure 2. The procedure and illustrations of parts of defect features extraction from X-ray CT data via CBIR techniques.

The basics of graph convolutional network

Graph convolutional network (GCN) is a deep learning model [18], which can combine the feature information and the graph structure to learn better representations of graphs via feature propagation and aggregation [19]. GCN consists of three parts: input layer, hidden layer, and output layer. In the input layer, the initial node representation is to be given. The GCN update the parameters of hidden layers to learn a better node representation and embed over training. The output layer can be used for (1) node classification, where the goal is to learn a representation vector so that the label can be predicted; (2) graph classification, where the set of graphs $\{G_1, \dots, G_N\} \subseteq \mathcal{G}$ is used to predict their labels $\{y_1, \dots, y_N\} \subseteq \mathcal{Y}$ of an entire graph [20]. Currently, GCN adopts a neighborhood aggregation strategy to iteratively update node representations by aggregating their neighborhood representations. GCN lays the foundation for investigating classification with the similarity information from features represented by the graph.

Hierarchical graph convolutional network

Hierarchical structure can incorporate various levels of information in the same structure for classification. We propose a hierarchical graph convolutional network (H-GCN) model for classification by a cascading GCN structure with a low-level and high-level features layer. GCN plays a significant role in building up our H-GCN model. Such an H-GCN leverages information from high-level and low-level features for classification and explores the impact of high-level features on low-level features and targets. In this model, we aim to learn representation vectors h_v of a node v such that its label can be classified as $\hat{y}_v = F(h_v)$. Graph representation is a technique to organize data in a graph structure with the relational knowledge of interacting entities [21]. H-GCN adopts the graph data structure to represent the relationship between different entities.

Definition 1 (Graph): the graph can be denoted as $G = (V, E)$, where V is the set of n nodes denoted as v_i with $v_i \in V, i = 1, \dots, n$, and E is the set of edges denoted as e_{ij} (the connection between v_i and v_j) with $e_{ij} = (v_i, v_j) \in E$. For node v_i , it contains a corresponding feature vector as $\mathbf{x}_i = [\mathbf{x}_i^H, \mathbf{x}_i^L]$, where $\mathbf{x}_i^H \in \mathbb{R}^e$ is a e -dimensional high-level feature vector, $\mathbf{x}_i^L \in \mathbb{R}^d$ is d -dimensional low-level feature vector. For convenience, we define high-level node feature matrix

$\mathbf{X}^H \in \mathbb{R}^{n \times e}$ stacks n high-level node feature on top of one another, $\mathbf{X}^H = [\mathbf{x}_1^H, \dots, \mathbf{x}_n^H]^T$ and low-level node feature matrix $\mathbf{X}^L \in \mathbb{R}^{n \times d}$ as $\mathbf{X}^L = [\mathbf{x}_1^L, \dots, \mathbf{x}_n^L]^T$. Each node is labeled with a C -dimensional vector $\mathbf{y}_i \in \{\mathbf{0}, \mathbf{1}\}^C$ via one-hot strategy. Two assumptions for H-GCN model are shown as:

Assumption 1: In graph G , each node $v_i \in V$ only denotes one sample and there is only one edge $e_{ij} \in E$ for every two nodes v_i and v_j . And the graph G is undirected, i.e., all of edges are bidirectional, which indicates that the adjacency matrix A is symmetric.

Assumption 2: Self-loop is allowed for the nodes in graph G which indicates that G is a simple graph in graph theory [22].

Definition 2 (Similarity matrix): the similarity matrix $\mathbf{S} \in \mathbb{R}^{n \times n}$ is adopted to measure the similarity between nodes v_i and v_j . In H-GCN, the similarity matrix $\mathbf{S} = \{s_{ij} | \forall i, j = 1, \dots, n\}$ is calculated by the Euclidean distance as

$$s_{ij} = \frac{1}{\|x_i - x_j\|^2} \forall i, j \in \{1, 2, \dots, n\}, \quad (1)$$

where \mathbf{x}_i and \mathbf{x}_j denotes the features of nodes v_i and v_j , respectively. For the similarity matrix, the smaller the distance between two nodes, the stronger the similarity among them. The Min-Max normalization is applied on the similarity matrix to obtain the normalized similarity matrix $\tilde{\mathbf{S}} = \{\tilde{s}_{ij} | \forall i, j = 1, \dots, n, \text{ and } 0 \leq \tilde{s}_{ij} \leq 1\}$ to facilitate the determination of edge connectivity. Additionally, in H-GCN model, the similarity matrixes of nodes with high-level features and low-level features are $\tilde{\mathbf{S}}_H$ and $\tilde{\mathbf{S}}_L$, respectively.

Definition 3 (Adjacency matrix): the adjacency matrix $\mathbf{A} \in \mathbb{R}^{n \times n}$ is a binary matrix which measures the connections between nodes v_i and v_j with 1 means connection and 0 is disconnection. It can be defined as $\mathbf{A} = \{a_{ij} | \forall i, j = 1, \dots, n\}$ where a_{ij} represents the connection between nodes v_i and v_j . The adjacency matrix \mathbf{A} is calculated as

$$a_{ij} = \begin{cases} 0, & \tilde{s}_{ij} > T \\ 1, & \tilde{s}_{ij} \leq T \end{cases}, \quad (2)$$

where T is the threshold to determine whether the distance among two nodes is smaller or not. In H-GCN, the distance threshold T among two nodes is given as the mid-point 0.5. Additionally, we define the diagonal degree matrix $\mathbf{D} = \text{diag}(d_1, \dots, d_n)$ where each value on the diagonal is the row-sum of adjacency matrix \mathbf{A} as $d_i = \sum_j a_{ij}$. In H-GCN model, the adjacency matrix with self-loop information is defined as $\mathbf{A}^* = \mathbf{A} + \mathbf{I}_n$ and degree matrix is $\tilde{\mathbf{D}} = \text{diag}(\tilde{d}_1, \dots, \tilde{d}_n)$, where $\tilde{d}_i = \sum_j a_{ij}^*$. The adjacency matrix of nodes with high-level features denotes \mathbf{A}_H^* and with low-level features is \mathbf{A}_L^* . Meanwhile, their degree matrixes are $\tilde{\mathbf{D}}_H$ and $\tilde{\mathbf{D}}_L$.

The progress of graph representation of H-GCN can be seen in Figure 3. The data is split into high-level features and low-level features and then two normalized similarity matrixes are calculated via the normalized Euclidean distance. Furthermore, adjacency matrix can be obtained from normalized similarity matrixes based on the threshold T . Finally, the high-level and low-level graphs are built which can be treated as the inputs of H-GCN.

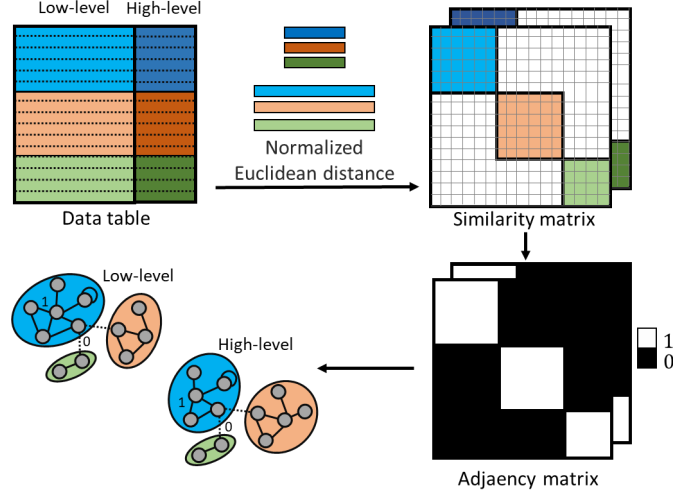


Figure 3. The progress of graph representations of H-GCN model.

We define a graph neural network GCN_1 with one hidden layer and one neuron in this layer to handle the high-level features to compress features and explore the impact of high-level features on low-level features and different classes of target. For the k -th graph layer in GCN_1 , we define matrix $\mathbf{H}_H^{(k-1)} = [h_1^{(k-1)}, \dots, h_v^{(k-1)}]^T$ as the high-level input node representations or embedding of all nodes and $\mathbf{H}_H^{(k)}$ as the low-level output node representations. The initial node representations can be expressed as

$$\mathbf{H}_H^{(0)} = \mathbf{X}^H, \quad (3)$$

which serve as the input to the first GCN_1 layer. Then the high-level features are input into the hidden layer of GCN_1 . The hidden layer is propagated layer by layer as:

$$\mathbf{H}_H^{(k)} = \text{ReLU}(\mathbf{U}_H \mathbf{H}_H^{(k-1)} \mathbf{W}_H^{(k-1)}), k = 1, \dots, K, \quad (4)$$

where $\mathbf{W}_H^{(k-1)} \in \mathbb{R}^{e \times p}$ is a learned weight matrix in this hidden layer with p neurons, and $\mathbf{U}_H \in \mathbb{R}$ denotes the “normalized” adjacency matrix constant with added self-loops as

$$\mathbf{U}_H = \tilde{\mathbf{D}}_H^{-\frac{1}{2}} \mathbf{A}_H^* \tilde{\mathbf{D}}_H^{-\frac{1}{2}}, \quad (5)$$

where $\tilde{\mathbf{D}}_H$ and \mathbf{A}_H^* are described in *Definition 3*.

After processing the high-level features, the output from high-level GCN_1 will be treated as the new input incorporated with low-level features \mathbf{X}^L into new input $\mathbf{X} = [\mathbf{X}^L, \mathbf{H}_H^{(K)}] \in \mathbb{R}^{n \times (d+p)}$. We adopt GCN_2 to train the low-level and new input features to explore the mixed impact of all features on different classes of targets. For the r -th graph layer in GCN_2 , the first input layer is

$$\mathbf{H}_L^{(0)} = \mathbf{X}, \quad (6)$$

The learned representation can be processed into the hidden layer of GCN_2 as

$$\mathbf{H}_L^{(r)} = \text{ReLU}\left(\mathbf{U}_L \mathbf{H}_L^{(r-1)} \mathbf{W}_L^{(r-1)}\right), r = 1, \dots, R, \quad (7)$$

where $\mathbf{W}_L^{(s-1)} \in \mathbb{R}^{(d+p) \times q}$ is a learned weight matrix in GCN₂ hidden layer with q neurons; \mathbf{U}_L is the normalized adjacency matrix as $\mathbf{U}_L = \tilde{\mathbf{D}}_L^{-\frac{1}{2}} \mathbf{A}_L^* \tilde{\mathbf{D}}_L^{-\frac{1}{2}}$.

For both of GCN₁ and GCN₂, in order to obtain the best weight matrix, we train by minimizing the cross-entropy loss function:

$$\text{loss} = -\sum_{i \in X} \sum_{j=1}^n \mathbf{y}_{ij} \ln \hat{\mathbf{y}}_{ij}, \quad (8)$$

For classification, the last layer of GCN₂ predicts the labels using a SoftMax classifier. We denote $\hat{\mathbf{Y}}_{HGCN} \in \mathbb{R}^{n \times C}$ where \hat{y}_v is the probability of node v to type c . The class prediction $\hat{\mathbf{Y}}$ of a R -layer GCN₂ can be written as

$$\hat{\mathbf{Y}}_{HGCN} = \text{softmax}\left(\mathbf{U}_L \mathbf{H}_L^{(R-1)} \mathbf{W}_L^{(R)}\right), \quad (9)$$

where $\text{softmax}(\cdot) = \exp(x) / \sum_{c=1}^C x_c$ is a normalizer across all types of targets and $\mathbf{W}_L^{(R)} \in \mathbb{R}^{q \times C}$ is the weights between GCN₂ layer and classification layer. In short, we can summarize the H-GCN model for classification in Algorithm 1 below.

Algorithm 1: The pseudo code of H-GCN

- Input:** High-level feature matrix $\mathbf{X}^H \in \mathbb{R}^{n \times e}$ and Low-level feature matrix $\mathbf{X}^L \in \mathbb{R}^{n \times d}$;
Output: $\hat{\mathbf{Y}}_{HGCN} \in \mathbb{R}^{n \times C}$;
- 1 Calculate normalized high-level and low-level similarity matrix $\tilde{\mathbf{S}}_H$ and $\tilde{\mathbf{S}}_L$ based on \mathbf{X}^H and \mathbf{X}^L in Equation (1).
 - 2 Obtain high-level adjacency matrix \mathbf{A}_H^* and low-level adjacency matrix \mathbf{A}_L^* based on the threshold T .
 - 3 Get high-level and low-level adjacency matrix operator as U_H and U_L , respectively.
 - 4 Initialize the weights matrixes $\mathbf{W}_H^{(k)} \in \mathbb{R}^{e \times p}$, $\mathbf{W}_L^{(r)} \in \mathbb{R}^{(d+p) \times q}$ and $\mathbf{W}_L^{(R)} \in \mathbb{R}^{q \times C}$ in GCN₁, GCN₂ and classifier respectively;
 - 5 **repeat**
 - 6 Update $\mathbf{W}_H^{(k)}$, input \mathbf{X}^H to train GCN₁ k -th hidden layer $\mathbf{H}_H^{(k)}$ based on U_H in Equation (4);
 - 7 Declare $\mathbf{X} = [\mathbf{X}^L, \mathbf{H}_H^{(k)}] \in \mathbb{R}^{n \times (d+p)}$, incorporate the output of GCN₁ $\mathbf{H}_H^{(k)}$ in K -th layer with \mathbf{X}^L ;
 - 8 Update $\mathbf{W}_L^{(r)}$, input \mathbf{X} to train GCN₂ r -th hidden layer $\mathbf{H}_L^{(r)}$ based on U_L in Equation (7);
 - 9 Update $\mathbf{W}_L^{(R)}$ and $\hat{\mathbf{Y}}_{HGCN}$, which is calculated by SoftMax function Equation (9);
 - 10 **until** loss function Equations (8) converges
-

Case study

The proposed H-GCN is applied to the L-PBF components for defects classification with real data, as well as exploring the impact of process parameters on different types of defects. In Section data collection, we collect different types of defect data and set the experiment for the L-PBF components. In Section L-PBF defect graph representations, we generate defect graphs via H-GCN based on defects data and process parameters in L-PBF. Finally, in Section analysis of H-GCN for defects classification, we adopt H-GCN for defects classification and evaluate the performance of H-GCN.

Data collection

In this case study, the effectiveness of the H-GCN model for defects classification of X-ray CT L-PBF specimens is verified with different L-PBF specimens fabricated with plasma atomized Ti-6Al-4V Grade 5 powder (particle size range of 15 to 53 μm) in an EOS M290 machine supplied by AP&C - a GE Additive company. The geometry of the X-ray CT specimens used in this case study and printed specimens are shown in Figure 4. In the fabrication process, the process parameters (except layer thickness) were modified from the manufactured recommended values to induce different types of volumetric defects. The EOS recommended process parameters for Ti-6Al-4V Grade 5 material are 280 W laser power, 1300 mm/sec laser speed, 40 μm layer thickness, and 120 μm hatch distance. The H-GCN model is validated by classifying three different types of defects, i.e., keyhole, LoF, and GEP of L-PBF specimens under eight combinations of process parameters shown in Table 2. Moreover, each specimen contains various defect samples for three types of defects in Table 3.

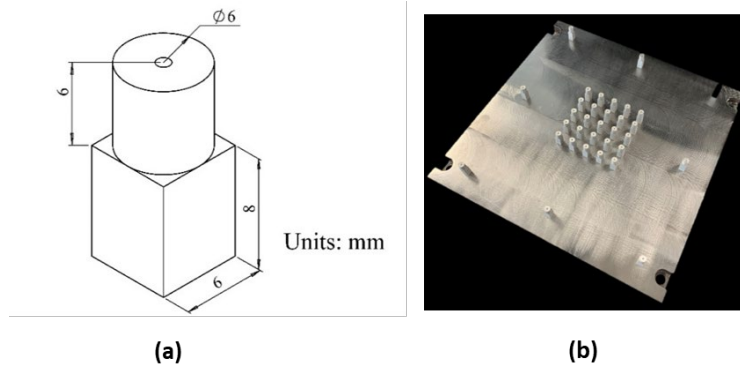


Figure 4. The geometry of the X-ray CT specimens (a) and the printed specimens (b).

Table 2. The different combinations of process parameters of specimens used in L-PBF experiments.

Process parameters	Units	Specimens							
		S23	S16	H24	H23	S11	K05	K03	K15
Laser power	W	224	252	280	280	280	336	336	364
Scanning speed	mm/s	1300	1560	1300	1300	1560	780	910	780
Hatch distance	μm	120	120	132	144	120	120	120	120
Layer thickness	μm	40	40	40	40	40	40	40	40

It is noted that each defect sample used in this study has 12 size and morphology-related features. The total defect data used in this study is 612 with 97 keyholes, 373 LoF, and 142 GEP. Furthermore, the proportion of training and test set for H-GCN and benchmark methods is 7:3. Additionally, all data are normalized to range [0,1] by min-max strategy before training and testing.

Table 3. The statistics for each type of defects for different specimens in L-PBF experiment.

Data	Total number of defects	Specimens							
		S23	S16	H24	H23	S11	K05	K03	K15
# of keyhole	97	-	-	-	-	-	68	4	25
# of LoF	373	74	92	36	69	77	25	-	-
# of GEP	142	2	-	3	7	2	122	6	-
Total	612	76	92	39	76	79	215	10	25

L-PBF defect graph representations

To build the L-PBF defect graph, we consider two aspects: (1) nodes and (2) edge connections. The L-PBF defects graph G is combined with two H-GCN graphs as a high-level graph G_H and a low-level graph G_L . We first discussed the high-level graph G_H consisting of high-level nodes only with three process parameters features and edge's connection. The edge's connection is based on the similarity between different nodes. As for the high-level edge's connection, the similarity of high-level defect nodes with process parameters features is calculated by Equation (1) and shown in Figure 5 (a). Based on this similarity, we apply the threshold of 0.5 to build the connection among high-level defect nodes (similarity < 0.5). The adjacency matrix of high-level defect nodes and their graph representation is shown in Figure 5 (b) and (c). In Figure 5, it is noted that the similarity within keyhole, LoF, and GEP is relatively large (the distance is small) compared with their cross area, which indicates that the defects with process parameters features have a potential relationship. It can also be reflected in its adjacency matrix and graph representation. We observe that almost all high-level defect nodes are connected with the same types of defects and only a few are associated with other types of defects. For example, the LoF defect nodes (green) in the middle of Figure 5 (c) are connected with LoF, GEP, and keyhole.

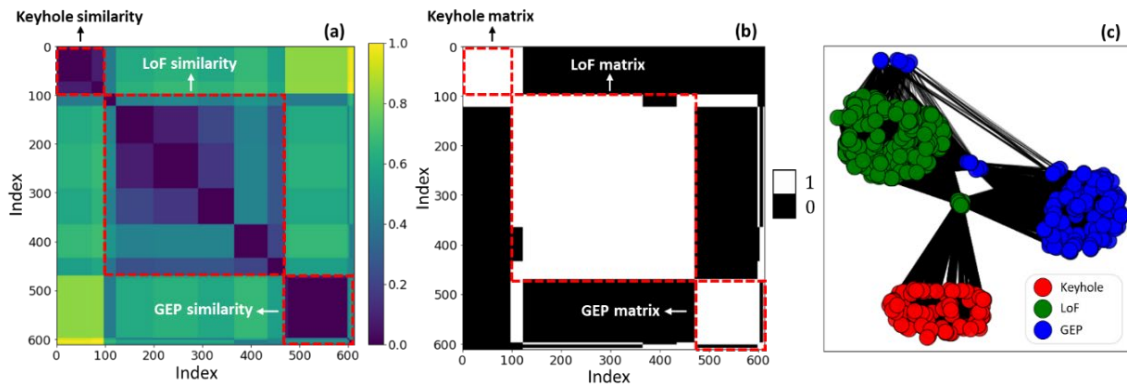


Figure 5. The similarity of defect nodes with high-level features and graph representation. (a) The similarity of defects with high-level features; (b) the adjacency matrix of defect nodes with high-level features; (c) the graph representation of nodes with high-level features.

The low-level graph G_L consists of low-level nodes only with 12 defect features and edge connections. Figure 6 (a) and (b) show the similarity of low-level defect nodes and their distributions. Critically, the threshold of 0.5 cutoff several connections within the keyhole, LoF and GEP similarity based on the results of their distribution which indicates that a few defects show no strong relationship with other the same types of defects.

Figure 6 demonstrates the adjacency matrix and low-level graph representation. It is noted that there are several connections among different types of defects in Figure 6 (a) which is reflected in Figure 6 (b). The number of connections between different types of defects is increased compared with the high-level graph. For example, there are more connections among keyhole, LoF and GEP in Figure 6 (b). The complete graph information for the high-level graph and the low-level graph can be seen in Table 4.

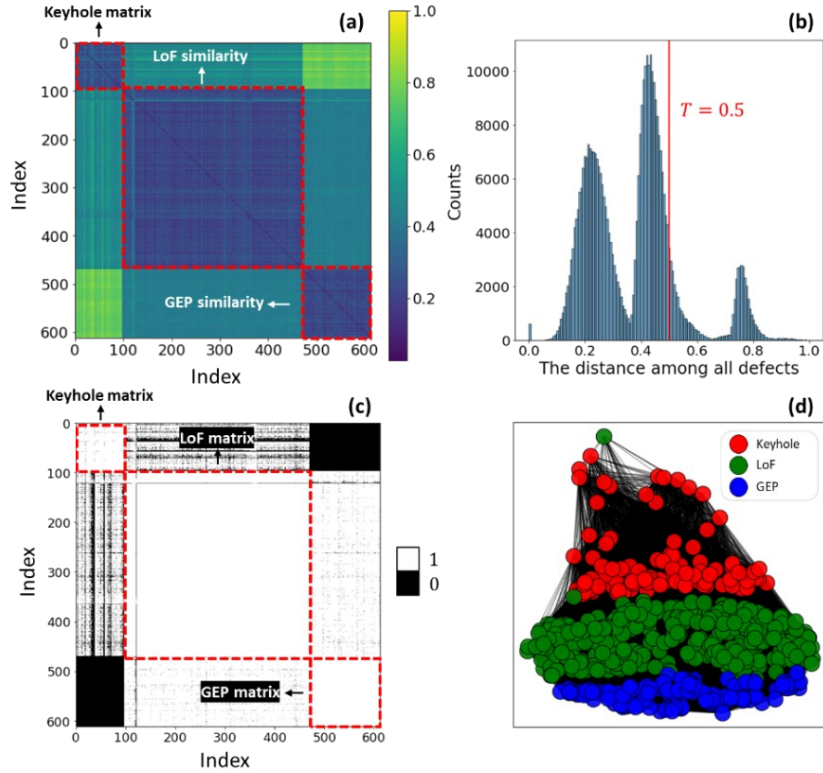


Figure 6. The similarity of defect nodes with low-level features. (a) The similarity of defects with low-level features; (b) the distribution of similarity matrix of low-level features; (c) the adjacency matrix of defect nodes with high-level features; (d) the graph representation of nodes with high-level features.

Table 4. The graph information of H-GCN for defects classification of L-PBF components.

Graph type	# Nodes	# Edges	Number of features for each node	Average node degree	Contains isolated nodes
H-GCN G_H	612	180584	3	295.07	False
H-GCN G_L	612	322574	12	527.08	False

Analysis of H-GCN for defects classification

As for the evaluation of H-GCN, three statistical metrics precision, recall and F1-score are used for evaluating the model classification performance. The proposed H-GCN is compared with GCN, neural network (NN), and support vector machine (SVM). The data used for comparison of H-GCN with other benchmark methods are as:

- **H-GCN:** adopts defect features + process parameters + similarity among defects.
- **GCN:** adopts defect features + similarity among defects.
- **NN and SVM:** adopt only defect features.

The mean and standard deviation of defect classification performance of the H-GCN and other benchmark methods are summarized in Table 5. It is noted that H-GCN significantly outperforms GCN, NN, and SVM for precision, recall and F1-score with all 1.000 without variance. Furthermore, we can observe from the confusion matrix in Figure 7 that NN and SVM are typically failed to classify LoF and GEP with some data shown in Figure 7 (c) and (d),

respectively. Moreover, GCN is better than NN and SVM for classifying all three types of defects, especially for GEP, without misclassified data because it uses additional edge connection information. Critically, H-GCN can classify keyhole, LoF, and GEP better than other methods without misclassified data for all types of defects since it adopts not only defect features but also process parameters and their similarity.

Table 5. The test classification results of H-GCN compared with other machine learning methods for L-PBF dataset (The values in the parenthesis are the standard deviation for all classes).

	H-GCN	GCN	NN	SVM
Precision	1.000	0.997 (0.0047)	0.970 (0.0216)	0.960 (0.0141)
recall	1.000	0.993 (0.0094)	0.953 (0.0386)	0.930 (0.0712)
F1-score	1.000	0.997 (0.0047)	0.963 (0.0236)	0.943 (0.0309)

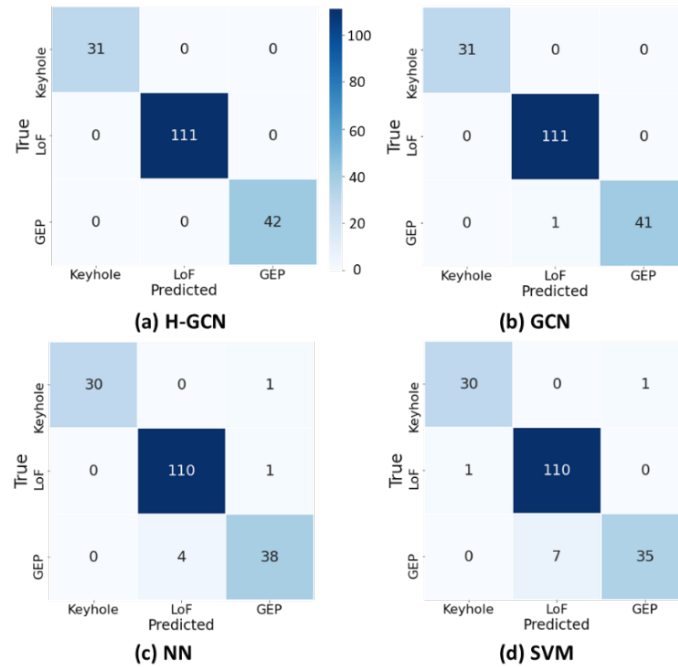


Figure 7. The comparison results of confusion matrix of H-GCN with other benchmark methods.

Discussion on impacts of process parameters on defects of L-PBF components

To explore the impact of process parameters on different types of defects of L-PBF specimens, we make further analyses for the weights of the H-GCN framework. The defects are typically correlated to the process energy and described by energy density E_v as a ratio among laser power (P), scanning speed (v), hatch distance (h), and layer thickness (δ) [23-26]:

$$E_v = \frac{P}{v \cdot \delta \cdot h}, [J/mm^3], \quad (10)$$

the layer thickness is a constant in this case study.

From our experiment for the study of weights of H-GCN, we found that the laser power is positively correlated with keyhole since the weight path is $(3.65) \rightarrow (-2.8) \rightarrow (-4.0)$ from laser power to keyhole. According to the Equation (10), we know that a higher laser power intends to inform keyhole defects. Additionally, LoF is induced by insufficient energy density defects which

is corresponded with the weight path of experimental result $(3.65) \rightarrow (-2.8) \rightarrow (3.01)$ from laser power to LoF and less laser power (low energy density) tends to increase GEP in the inner structure of L-PBF specimens with two weight paths $(3.65) \rightarrow (-0.4) \rightarrow (4.54)$ and $(3.65) \rightarrow (-2.8) \rightarrow (0.8)$ from laser power to GEP.

Conclusion and future work

This research develops a novel H-GCN model for defect classification of L-PBF components using a graph representation of data in a layer-by-layer GCN structure to build the multilevel multifactorial model. Specifically, H-GCN first incorporates process parameters and defect features observed from X-ray CT scans into high-level and low-level graphs, respectively, based on the similarity of defects. The similarity information considers the relationship among defects and improves the accuracy of defect classification. Furthermore, H-GCN adopts two GCNs for high-level and low-level graphs to make highly accurate defect classification. This hierarchical structure of H-GCN enables its flexible scalability. Multilevel information can be processed hierarchically by H-GCN to account for differences and interactions among different level data. This work achieves perfect defect classification of L-PBF components with a statistical F1-score of 1.000. Compared with other models such as SVM, its performance improves by about 6%.

The future work of H-GCN includes: (1) to extend the hierarchical structure of H-GCN to cases with multilevel multifactorial modeling; (2) to apply H-GCN to other fields and find new applications in a broader range of disciplines, such as drug design in chemistry, cancer subtype classification in biology, and social relationship understanding in social media.

References

- [1] S. Ford and M. Despeisse, "Additive manufacturing and sustainability: an exploratory study of the advantages and challenges," *Journal of cleaner Production*, vol. 137, pp. 1573-1587, 2016.
- [2] N. Guo and M. C. Leu, "Additive manufacturing: technology, applications and research needs," *Frontiers of mechanical engineering*, vol. 8, no. 3, pp. 215-243, 2013.
- [3] S. K. Everton, M. Hirsch, P. Stravroulakis, R. K. Leach, and A. T. Clare, "Review of in-situ process monitoring and in-situ metrology for metal additive manufacturing," *Materials & Design*, vol. 95, pp. 431-445, 2016.
- [4] M. Abdelwahed, "Development and L-PBF processing of structural low-alloy steels for automotive applications," 2022.
- [5] M. S. Kumar, H. Javidrad, R. Shanmugam, M. Ramoni, A. A. Adediran, and C. I. Pruncu, "Impact of print orientation on morphological and mechanical properties of L-PBF based AlSi7Mg parts for aerospace applications," *Silicon*, pp. 1-15, 2021.
- [6] N. Ahmed, I. Barsoum, G. Haidemenopoulos, and R. A. Al-Rub, "Process parameter selection and optimization of laser powder bed fusion for 316L stainless steel: A review," *Journal of Manufacturing Processes*, vol. 75, pp. 415-434, 2022.
- [7] S. Bhat and R. Patibandla, "Metal fatigue and basic theoretical models: a review," *Alloy steel-properties and use*, vol. 22, 2011.
- [8] A. J. Sterling, B. Torries, N. Shamsaei, S. M. Thompson, and D. W. Seely, "Fatigue behavior and failure mechanisms of direct laser deposited Ti-6Al-4V," *Materials Science and Engineering: A*, vol. 655, pp. 100-112, 2016.
- [9] U. Zerst, M. Madia, C. Klinger, D. Bettge, and Y. Murakami, "Defects as a root cause of fatigue failure of metallic components. I: Basic aspects," *Engineering Failure Analysis*, vol. 97, pp. 777-792, 2019.

- [10] W. H. Kan *et al.*, "A critical review on the effects of process-induced porosity on the mechanical properties of alloys fabricated by laser powder bed fusion," *Journal of Materials Science*, pp. 1-48, 2022.
- [11] J. Pegues, M. Roach, R. S. Williamson, and N. Shamsaei, "Volume effects on the fatigue behavior of additively manufactured Ti-6Al-4V Parts," in *2018 International Solid Freeform Fabrication Symposium*, 2018: University of Texas at Austin.
- [12] E. Pessard, M. Laviolle, P. Laheurte, P. Didier, and M. Brochu, "High-cycle fatigue behavior of a laser powder bed fusion additive manufactured Ti-6Al-4V titanium: Effect of pores and tested volume size," *International Journal of Fatigue*, vol. 149, p. 106206, 2021.
- [13] W. Cui, Y. Zhang, X. Zhang, L. Li, and F. Liou, "Metal additive manufacturing parts inspection using convolutional neural network," *Applied Sciences*, vol. 10, no. 2, p. 545, 2020.
- [14] Y. Mingqiang, K. Kidiyo, and R. Joseph, "A survey of shape feature extraction techniques," *Pattern recognition*, vol. 15, no. 7, pp. 43-90, 2008.
- [15] A. Li, S. Baig, J. Liu, S. Shao, and N. Shamsaei, "Defect Criticality Analysis on Fatigue Life of L-PBF 17-4 PH Stainless Steel via Machine Learning," *International Journal of Fatigue*, p. 107018, 2022.
- [16] H. Wadell, "Sphericity and roundness of rock particles," *The Journal of Geology*, vol. 41, no. 3, pp. 310-331, 1933.
- [17] H. Parameswaran, E. Bartolák-Suki, H. Hamakawa, A. Majumdar, P. G. Allen, and B. Suki, "Three-dimensional measurement of alveolar airspace volumes in normal and emphysematous lungs using micro-CT," *Journal of Applied Physiology*, vol. 107, no. 2, pp. 583-592, 2009.
- [18] T. N. Kipf and M. Welling, "Semi-supervised classification with graph convolutional networks," *arXiv preprint arXiv:1609.02907*, 2016.
- [19] F. Scarselli, M. Gori, A. C. Tsoi, M. Hagenbuchner, and G. Monfardini, "The graph neural network model," *IEEE transactions on neural networks*, vol. 20, no. 1, pp. 61-80, 2008.
- [20] K. Xu, W. Hu, J. Leskovec, and S. Jegelka, "How powerful are graph neural networks?," *arXiv preprint arXiv:1810.00826*, 2018.
- [21] W. L. Hamilton, R. Ying, and J. Leskovec, "Representation learning on graphs: Methods and applications," *arXiv preprint arXiv:1709.05584*, 2017.
- [22] D. B. West, *Introduction to graph theory*. Prentice hall Upper Saddle River, 2001.
- [23] H. Gong, K. Rafi, H. Gu, T. Starr, and B. Stucker, "Analysis of defect generation in Ti-6Al-4V parts made using powder bed fusion additive manufacturing processes," *Additive Manufacturing*, vol. 1, pp. 87-98, 2014.
- [24] T. Vilaro, C. Colin, and J.-D. Bartout, "As-fabricated and heat-treated microstructures of the Ti-6Al-4V alloy processed by selective laser melting," *Metallurgical and materials transactions A*, vol. 42, no. 10, pp. 3190-3199, 2011.
- [25] B. Vrancken, L. Thijs, J.-P. Kruth, and J. Van Humbeeck, "Heat treatment of Ti6Al4V produced by Selective Laser Melting: Microstructure and mechanical properties," *Journal of Alloys and Compounds*, vol. 541, pp. 177-185, 2012.
- [26] L. Thijs, F. Verhaeghe, T. Craeghs, J. Van Humbeeck, and J.-P. Kruth, "A study of the microstructural evolution during selective laser melting of Ti-6Al-4V," *Acta materialia*, vol. 58, no. 9, pp. 3303-3312, 2010.
- [27] J. Xiong, Z. Xiong, K. Chen, H. Jiang, and M. Zheng, "Graph neural networks for automated de novo drug design," *Drug Discovery Today*, vol. 26, no. 6, pp. 1382-1393, 2021.
- [28] S. Rhee, S. Seo, and S. Kim, "Hybrid approach of relation network and localized graph convolutional filtering for breast cancer subtype classification," *arXiv preprint arXiv:1711.05859*, 2017.
- [29] Z. Wang, T. Chen, J. Ren, W. Yu, H. Cheng, and L. Lin, "Deep reasoning with knowledge graph for social relationship understanding," *arXiv preprint arXiv:1807.00504*, 2018.